Effects of long jumps, reversible aggregation, and Meyer-Neldel rule on submonolayer epitaxial growth

A. Beausoleil, P. Desjardins, and A. Rochefort
Regroupement québécois sur les matériaux de pointe (RQMP) and Department of Engineering Physics, École Polytechnique de Montréal, Montréal, (Québec), Canada

(Received 3 March 2008; revised manuscript received 7 July 2008; published 13 August 2008)

We demonstrate, using kinetic Monte Carlo simulations of submonolayer epitaxial growth, that long jumps and reversible aggregation have a major impact on the evolution of island morphologies. Long jumps are responsible for a supra-Arrhenius behavior of the effective diffusion coefficient as the attachment and detachment kinetics give rise to a bimodal island size distribution that depends on temperature and long jump extent limits. As the islands density increases with temperature, the average size of stable islands reaches a maximum before decreasing. We have also observed that the diffusion coefficient cannot be used alone to predict the evolution of island sizes and morphologies, the relative rate of each process having a major importance. Our theoretical developments are of direct relevance for materials systems such as Au, Pd, Ag, Cu, Ni, H/Si, H/W(110), Co/Ru, and Co/Ru(S), that are known for exhibiting a compensation effect that cannot be contained within experimental uncertainties.

DOI: 10.1103/PhysRevE.78.021604 PACS number(s): 81.15.Aa, 68.35.Fx, 68.55.A−

I. INTRODUCTION

According to the transition state theory (TST), the rate of activation of a diffusion event follows an Arrhenius behavior in the harmonic approximation [1]. That is, if the activation energy is E, the rate is

$$\Gamma = \Gamma_0 e^{-E/k_B T},$$

where Γ_0 is the attempt frequency or prefactor, T is the temperature, and k_B is the Boltzmann constant.

In 1995, Boisvert *et al.* [2] have shown with an embedded-atom-method molecular-dynamics study that the compensation law or the Meyer-Neldel rule (MNR) could describe self-diffusion rates on Au, Pd, Ag, Cu, and Ni. This rule states that the diffusion rate of an event with an activation energy E_i writes

$$\Gamma_i = \Gamma_{i,0}(E_i) e^{-E_i/k_B T}, \tag{1}$$

with the prefactor $\Gamma_{i,0}$ depending on the activation energy as

$$\Gamma_{i,0}(E_i) = \Gamma_{00} e^{(E_i/k_B T_{\mathrm{iso}})^{\varepsilon}}. \tag{2}$$

Γ_{00} is the constant part of the prefactor, ε is a constant ranging between $1/2$ and 1 that depends on the nature of the fundamental excitations [3], and T_{iso} is the isokinetic temperature at which all diffusion events should have an identical rate.

According to the multiple excitation entropy (MEE) model [4], two conditions must be fulfilled to ensure that the MNR applies. That is, the activation energy must be large with respect to the (i) thermal and (ii) elementary excitation energies. Since $k_B T_{\mathrm{iso}}$ is of the order of the elementary excitation energies [4], we can write both conditions as $E_i \gg k_B T$ and $E_i \gg k_B T_{\mathrm{iso}}$. The impacts of this law should be more clearly observed in systems at temperatures near T_{iso}. Indeed, as the temperature increases, the rate of high activation energy processes increases much more rapidly than that for low energy processes. At high temperature near T_{iso}, the high energy processes, such as the correlated long jumps in epitaxial crystal growth, significantly contribute to the total rate of processes. This behavior might considerably affect the surface topography.

Many approaches are possible for understanding and predicting the long jumps phenomenon. Jacobsen *et al.* [5] developed a transition path theory to determine the path of long jumps between second nearest neighbors. They used molecular-dynamics to determine that the prefactor is a function of the temperature (proportional to $\sqrt{T}$ in one dimensional diffusion). Montalenti and Ferrando [6] linked long jumps to the potential energy surface and could explain the important differences in the behavior of long jumps observed between (110) surfaces of Cu, Ag, and Au although the activation energies of single hops do not show a large variation between the three surfaces. Long jumps can also be linked to surface friction because adatoms exchange energy with the surface. When the friction per unit mass η is small enough, long jumps are more likely. Ferrando *et al.* established what vibrational frequencies and activation energy conditions are required to allow significant long jumps [7]. Assuming a Brownian motion, Chen and Ying [8] solved the equation of movement for an atom subject to friction and reacting to stochastic forces (the Langevin equation) and determined the probability of long jumps for a given friction coefficient, assuming that $k_B T$ is much lower than the potential barrier E_d.

Since long jumps have been shown to have non-negligible probabilities on several surfaces [9–11], their contribution must be considered. For Ag and Au (100) and (111) surfaces, Boisvert and Lewis [12] have shown, using molecular-dynamics simulations within an embedded-atom approach, that correlated long jumps contribute to increase the diffusion coefficient, which then no longer exhibits an Arrhenius behavior. Within a 1D analysis, they find that the diffusion coefficient for long jumps of any extent ℓ for a (100) surface is

$$D^{1D}_{\ell<\infty} = D^{1D}_{\ell=1}\left(\frac{1+e^{-\beta}}{1-e^{-\beta}}\right),$$

where $\beta = E_d/k_BT$, with E_d, the diffusion energy barrier. $D^{1D}_{\ell=1}$ is the 1D diffusion coefficient on the (100) surface when only random walk, that is, between nearest neighbors (NNs), is considered. The diffusion coefficient can be found with the Einstein equation

$$D_{\ell=1} = \lim_{t\to\infty}\frac{\langle R_{\ell=1}(t)^2\rangle}{\upsilon t},$$

where $\langle R_{\ell=1}(t)^2\rangle$ is the mean square displacement of an adatom making a single hop after a time t, and υ is the maximum number of in-plane NNs [e.g., four for a simple cubic (100) surface]. While the 1D analysis gives some insight on the overall trends, a 2D treatment needs to be considered to completely describe the impact of long jumps on the evolution of island sizes and morphologies during growth. In addition to a greater contribution of long jumps to the total process rates near the isokinetic temperature, the detachment of adatoms, which is less likely to occur at low temperature, can become sufficiently important near T_{iso} to cause a reversible aggregation. Rate equations and kinetic Monte Carlo (KMC) models have been used to study such a regime [13,14]. Using a KMC model, Ratsch *et al.* [13] reproduce experimental results for Au/Ru(0001) and Ni/Ni(100). They observe an increasing density of islands, which is more precisely related to a larger number of small islands.

For simplicity purposes, the analysis performed to describe the evolution of island sizes and morphologies from experimental or simulated crystal growth data is frequently based on the following assumptions: aggregation is irreversible, diffusion coefficient follows an Arrhenius behavior, the attempt frequency of a diffusion event is constant for every process, and the rate of long jumps is so low with respect to the single hop rate that they can be completely neglected. While such assumptions might be relevant for growth at a low temperature, a much different behavior might be observed at high temperatures where the relative difference between the rates of the various processes decrease. This is even more important when the MNR is taken into account.

The present paper focuses on the impact of high energy processes—that may be enhanced by the MNR—on island sizes and morphologies. Our main goal is not to support a universal application of the MNR, but to concentrate on surfaces which have shown compensation effects, such as homoepitaxy on Au, Pd, Ag, Cu, and Ni surfaces [2]. Similarly, the growth of Co on Ru(0001) is a system in which the important lateral interactions between adsorbed atoms [16] can lead to important compensation effects [17]. Another example concerns the growth of Co on a vicinal sulfided Ru surface [18], where the diffusion preexponential factor along terraces is more than two orders of magnitude higher than that over the steps while the activation energy of the latter is approximately twice that of the former. Adsorption of H on Si [19] and isotopes of H on W(110) [20] also reveals compensation effects.

Although it has been shown that other compensation effects can occur with the number of atoms involved in concerted atomic processes [21], we concentrate our work on single atomic motions (single atom diffusion) for simplicity.

We show that when the MNR applies, (i) the supra-Arrhenius behavior predicted for the diffusion coefficient is amplified, and (ii) a bimodal island size distribution is enhanced at high temperatures because of the reversible aggregation regime.

II. MODEL

To observe the impact of high activation energy processes when the temperature increases, we allow long jump events and detachment in addition to free diffusion, edge diffusion, and diffusion across steps. The relative energy of each process is determined using a simple bond counting model. This allows one to obtain general equations for long jump probabilities and the diffusion coefficient. To observe their individual impact, the MNR, long jumps, and detachment events can be tuned off separately.

A. Long jumps

During the last decade, it has been theoretically [8,12] and experimentally [22] shown that long jumps have an activation energy that increases linearly, at least in some cases, with the length of the jump. Since we consider long jumps as a combination of single hopping events, the activation energy should increase with the total jump path length. Our model thus forbids backward hops (as part of long jumps) because they require one to define an additional energy due to their longer path. This phenomenon should therefore be negligible with respect to straightforward jumps.

We then introduce the notion of *extent*, which is equivalent to the path length when backward hops are forbidden. While the *length* of a jump is the distance between the starting and arrival points, the *extent* of the jump is the minimal number of single hops required to reach the arrival point. On a Cartesian grid within the solid-on-solid (SOS) approximation where the end point is located at coordinates $(\Delta x, \Delta y)$ from the starting point, the *extent* is $\ell = |\Delta x| + |\Delta y|$.

While the starting and arrival points are connected by a single path for single hops, many paths are possible for long jumps. This path multiplicity leads to a different arrival probability for each accessible site. If we note p_i the probability of a jump of extent i following a single path, the global probability pattern for long jumps with an extent limit ℓ_{max} [23] of four atomic units is illustrated in Fig. 1. For example, in Fig. 1, the dotted arrows correspond to three different paths connecting the same starting and arrival points. Each of these long jump paths have a probability p_3 and the *total* probability for this long jump is $3p_3$ (the single path probability multiplied by the number of different paths). Our model includes such an additional entropic contribution, which is not in contradiction with the MEE model [4].

Owing to their dependence on surface friction, Chen *et al.* conclude that indirect long jumps experience more friction and are less likely to occur than direct jumps [24], the former being retrapped more easily. That is, performing a long jump with $|\Delta x|, |\Delta y| < \ell$ should be less favorable than a jump with

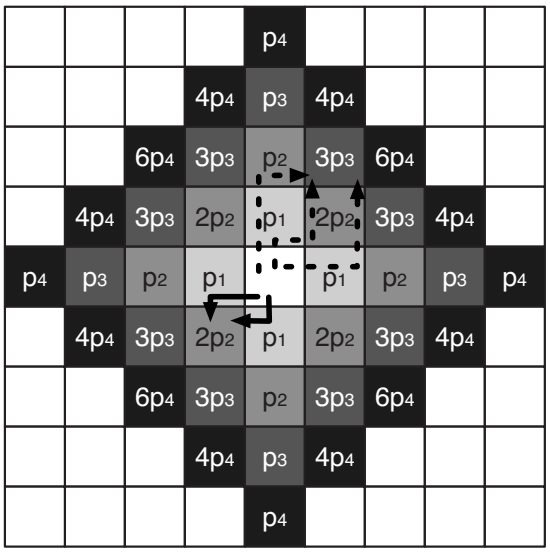

FIG. 1. Jump probabilities pattern for a single adatom in the center of the grid. Each square is an accessible site according to the SOS model. Sites from light gray to black represent sites accessible by jumps of 1, 2, 3, or 4 *extent* atomic units, respectively. p_i is the probability of a long jump of extent i for a single path. The arrows show the path multiplicity for two different sites.

$|\Delta x|=\ell$ or $|\Delta y|=\ell$. However, considering the path followed by long jumps of Ir or W on W(110), Antczak and Ehrlich observed experimentally that the rates of direct and indirect jumps were of the same order [10]. Therefore, to keep our model simple, we define long jumps as a combination of single hops so that p_ℓ is the same for every path of a given jump of extent ℓ.

B. Bond counting

To simplify the theoretical treatment of different processes, we use a simple bond counting model, assuming that energy barriers vary with the number of in-plane NNs before (n_i) and after (n_f) the diffusion event, which is a widely used approach in bond counting KMC simulations [25]. The difference n_i-n_f allows one to favor attachment at high coordination sites (e.g., kinks compared to flat step edges) and to prevent detachment from those sites. We further assume that the energy barriers can be derived from the following equation:

$$\Delta E = n_i E_0 + (n_i - n_f)E_\Delta + \ell E_\ell + n_\uparrow E_\uparrow + n_\downarrow E_{\mathrm{ES}}, \qquad (3)$$

where ℓ is the extent of the jump in atomic units, $n_\uparrow$ is the number of atomic height steps to climb from the initial to the final state, and $n_\downarrow$ is the number of times a step of any height an adatom has to descend to get to the final state. E_0 and E_Δ favor the attachment of adatoms to the islands, E_ℓ is the additional energy needed to increase the extent of the long jump by one atomic unit, $E_\uparrow$ is the energy needed to climb over a monolayer step, and E_{ES} is the Ehrlich-Schwoebel barrier [26,27]. A minimal energy of $E_{\min}=E_\ell-\upsilon E_\Delta$ is associated to every event, where υ is the maximum number of NNs in the plane of the atom in the final state [the same value as the one used in Eq. (3)] and the energy of diffusion between NNs is $E_d=E_\ell$. This model thus establishes a difference between diffusion on a terrace and diffusion across steps. The attachment of adatoms to islands is favored with respect to the detachment, and the probability of single hopping events is larger than that for long jumps.

When Eq. (3) is applied integrally, the reversible aggregation (RA) mode is modeled. We define some other levels of aggregation reversibility following two conditions with respect to the bond counting model parameters. The first condition is that if $n_i>n_i^0$, atoms cannot detach from islands. The second condition is that if $n_i>n_i^0$, attached atoms can only move along island edges. With those conditions, we associate $n_i^0=1$ with the first level of reversibility (RA1 mode) and $n_i^0=2$ with the second (RA2 mode). In the third, $n_i^0=3$, which is the case for the reversible aggregation mode (RA mode) on a Cartesian grid using the SOS approximation. When $n_i^0=0$, the irreversible aggregation (IA) mode is modeled. That is, for the IA mode, once an atom is attached to an island, it cannot detach from it. For the RA1 (RA2) mode, atoms surrounded by two (three) NNs or more cannot detach from an island. In the RA mode, atoms must have four NNs to be fixed. The critical island size is not fixed in our study since we treat every island edge in a microstructural way by counting the in-plane NNs. Therefore, whenever the aggregation mode allows it, atoms can detach from islands of every size.

C. Long jump probabilities and diffusion coefficient

Our bond counting model allows one to write equations for (i) the relative probability of performing long jumps with respect to single hopping events and (ii) the diffusion coefficient of a single adatom on a flat surface.

For an adatom centered on the Cartesian grid shown in Fig. 1, the probability P of presence at $(\Delta x,\Delta y)$ after one diffusion event is

$$P(\Delta x,\Delta y) = \frac{(|\Delta x|+|\Delta y|)!}{|\Delta x|\,!\,|\Delta y|!} p_{(|\Delta x|+|\Delta y|)},$$

with p_ℓ [where $\ell=(|\Delta x|+|\Delta y|)$] being the probability of a jump of extent ℓ following a single path as defined earlier.

We can rewrite this equation noting that the right-hand-side ratio, which corresponds to the path multiplicity, is a binomial coefficient,

$$P(\Delta x,\Delta y) = \binom{|\Delta x|+|\Delta y|}{|\Delta x|} p_\ell = \binom{\ell}{|\Delta x|} p_\ell.$$

Therefore, the total probability for a long jump of extent ℓ to occur is

$$P_\ell = 4\sum_{\Delta x=0}^{\ell-1} \binom{\ell}{|\Delta x|} p_\ell = 4(2^\ell - 1)p_\ell, \qquad (4)$$

where the fact that

$$P(\Delta x,\Delta y) = P(-\Delta x,-\Delta y) = P(\Delta y,-\Delta x) = P(-\Delta y,\Delta x)$$

was used to simplify the summation in Eq. (4).

The normalization of Eq. (4) implies that

$$\sum_{\ell=1}^{\ell_{\max}} P_\ell = 1. \tag{5}$$

We consider explicitly the MNR as expressed in Eq. (2) and assume $\varepsilon=1$, which represents elementary excitations originating from electrons and optical phonons [3]. Other values of ε can easily be included in the model. For the bond counting model defined by Eq. (3), the energy barrier for adatom diffusion over an extent ℓ becomes $\Delta E_\ell = \ell E_\ell$ and the single path probability is

$$p_\ell = k_{\ell\le\ell_{\max}}\Gamma_\ell = k_{\ell\le\ell_{\max}}\Gamma_{00}e^{-\alpha\ell},$$

where $\alpha=\frac{E_\ell}{k_B}(\frac{1}{T}-\frac{1}{T_{\text{iso}}})$ and $k_{\ell\le\ell_{\max}}$ is a proportionality constant that depends on the jump extent limit. In this case, Eq. (5) allows one to define $k_{\ell\le\ell_{\max}}$ as follows:

$$k_{\ell\le\ell_{\max}} = \begin{cases} \dfrac{1}{4\Gamma_{00}(2^{\ell_{\max}+1}-\ell_{\max}-2)} & \text{if } \alpha=0 \\ \dfrac{2^{\ell_{\max}}}{4\Gamma_{00}(2^{\ell_{\max}}[\ell_{\max}-1]+1)} & \text{if } \alpha=\ln(2) \\ \dfrac{e^{\alpha}(1-e^{-\alpha})(1-2e^{-\alpha})}{4\Gamma_{00}(1-e^{-\alpha\ell_{\max}}[2^{\ell_{\max}+1}\{1-e^{-\alpha}\}-\{1-2e^{-\alpha}\}])} & \text{elsewhere,} \end{cases}$$

and

$$k_{\ell<\infty} = \frac{(1-e^{-\alpha})(1-2e^{-\alpha})}{4\Gamma_{00}e^{-\alpha}}, \quad \text{if } \alpha>\ln(2).$$

Since we restrict the simulation domain of α to be coherent with the MEE model, the condition $\alpha>\ln(2)$ will always be fulfilled and we will omit to recall this condition in the following. We briefly mention that k_∞ is discontinuous for $\alpha\le\ln(2)$ because the total probability of performing long jumps would increase with the extent of the jump.

We can now write an explicit equation for the total probability of performing a jump of extent ℓ as follows:

$$P_\ell = \frac{(2^\ell-1)e^{-\alpha(\ell-1)}(1-e^{-\alpha})(1-2e^{-\alpha})}{1-e^{-\alpha\ell_{\max}}(2^{\ell_{\max}+1}[1-e^{-\alpha}]-[1-2e^{-\alpha}])}, \tag{6}$$

$$P_\ell^\infty = \lim_{\ell_{\max}\to\infty} P_\ell = (2^\ell-1)\frac{(1-e^{-\alpha})(1-2e^{-\alpha})}{e^{\alpha(\ell-1)}}. \tag{7}$$

Equations (6) and (7) consider the MNR and the path multiplicity of long jumps. However, if such parameters are neglected, the results of Boisvert and Lewis [12], and of Chen and Ying [8], which give $P_\ell^\infty=(e^\beta-1)e^{-\ell\beta}$, are reproduced.

When the extent limit $\ell_{\max}$ is finite, the cumulated probability $\delta_{\ell\le\ell_{\max}}$ of neglected jumps with respect to an infinite extent is an explicit function of $\ell_{\max}$ according to

$$\delta_{\ell\le\ell_{\max}} = 1-\sum_{\ell=1}^{\ell_{\max}} P_\ell^\infty = \frac{(2^{\ell_{\max}+1}-1)-(2^{\ell_{\max}+1}-2)e^{-\alpha}}{e^{\alpha\ell_{\max}}}. \tag{8}$$

The $\delta_{\ell\le\ell_{\max}}$ parameter allows one to determine the difference on the total number of jumps due to the finite extent of jumps. For $\alpha>\ln(2)$, $\delta_{\ell\le\ell_{\max}}$ decreases with $\ell_{\max}$.

We show in Appendix A that $D_{\ell\le\ell_{\max}}$, the diffusion coefficient for a finite jump extent limit, can be written with respect to $D_{\ell=1}$, the diffusion coefficient for single hopping events (random walk). That is,

$$D_{\ell\le\ell_{\max}} = D_{\ell=1}\nu_{\ell\le\ell_{\max}}, \tag{9}$$

with $D_{\ell=1}=a^2\Gamma_{00}e^{-\alpha}$, and $\nu_{\ell\le\ell_{\max}}$ a scaling factor that depends on $\ell_{\max}$ and α [see Eqs. (A1) and (A3)–(A7) in Appendix A].

Since the diffusion coefficient is one of the dominant factors that determine the topography of a surface, we evaluate the relative difference between finite and infinite long jump extent limits

$$\Upsilon_{\ell\le\ell_{\max}} = \frac{D_{\ell<\infty}-D_{\ell\le\ell_{\max}}}{D_{\ell<\infty}} = \frac{\nu_{\ell<\infty}-\nu_{\ell\le\ell_{\max}}}{\nu_{\ell<\infty}}. \tag{10}$$

We end this section by recalling that our model is two-dimensional and considers a path multiplicity. In the absence of a path multiplicity, the diffusion coefficient increases less rapidly with increasing temperature. If only one dimensional diffusion is allowed, we obtain the theoretical results of Boisvert and Lewis [12] with the difference that our model considers explicitly the MNR [28]. We emphasize the fact that the results presented here are valid even for systems where MNR does not apply, except that the evolution of the diffusion coefficient would be closer to the Arrhenius behavior.

This similitude between results considering or not the MNR is due to the fact that there exist temperature and flux conditions which give the same surface evolution in both cases. Those conditions are derived in Appendix B. More precisely, all surface evolutions of simulations that do not consider the MNR are reproduced by simulations that do consider the MNR, but the reverse is not true.

III. METHODOLOGY AND COMPUTATIONAL DETAILS

The theoretical developments of Sec.II C and Appendix A assume a single adatom diffusing on a flat surface. To evaluate the validity of those developments when many adatoms and islands are present on the surface, we use the kinetic Monte Carlo method (KMC) as formulated by the Bortz, Kalos, and Lebowitz (BKL) model [30]. The KMC code allows to simulate the evolution of simple cubic (100) surfaces using the SOS approximation.

In KMC, events are considered as Poisson processes. Therefore, the average time between two successive events is

$$\langle \Delta t \rangle = 1/\mathbf{R}(t), \tag{11}$$

where $\mathbf{R}(t)=[F(t)abL_xL_y+\Sigma_i\Gamma_i]$ is the total rate of possible events on the surface at a given time. $F(t)$ is the uniform adatom flux (in $1/\mathrm{m}^2\,\mathrm{s}$) on the surface, $L_x \times L_y$ are the SOS grid dimensions, and a and b are the surface atomic units for a Cartesian grid. Γ_i values are the rates of all possible processes on the surface at a given time. Two uniform random number generators are used in our KMC simulations: one integer [31] to choose the location of a deposition event and one real from a Mersenne Twister algorithm [32] to choose the event to perform. The former has a $\delta r < 2.3 \times 10^{-10}$ resolution.

Our simulations were done for a simple cubic (100) surface ($b=a$) with a global flux of $Fa^2=0.1$ ML/s and periodic boundary conditions. Simulations were stopped at a coverage of $\theta=0.2$ ML (total simulation time of $t_{\mathrm{tot}}=\theta/Fab=2$ s). The size of the simulation grid was $L_x \times L_y=250 \times 250$. We also make use of normalized coordinates in the simulation by setting $a=1$.

In Sec. II C, we have derived a set of equations for the diffusion coefficient of a single adatom on a flat surface. In the KMC simulations, more than one adatom is diffusing simultaneously and the application of the Einstein equation is not straightforward. In order to evaluate an *effective* diffusion coefficient in the presence of many atoms, we perform a linear regression on adatoms following

$$D' = \frac{\sum_i R(t_i)^2 t_i}{v \sum_i t_i^2}, \tag{12}$$

where t_i and $R(t_i)^2$ are, respectively, the diffusion time and the square distance of diffusion before the attachment of adatom i. The prime symbol is used to distinguish the effective diffusion coefficient from the theoretical one.

The parameters of the preceding equation are collected as follows. When an adatom is created (by deposition or by detachment from an island), its original position and the simulation time are recorded. Just before the attachment to an island, the total distance of diffusion and the corresponding simulation time are recorded. Therefore, only the contribution of adatoms that attach to an island edge or nucleate is compiled to find the effective diffusion coefficient.

While Eq. (12) allows one to find a good approximation of the real diffusion coefficient, some discrepancies appear in many situations. Among others, let us mention the compactness and average size of islands, the time the simulation time step takes to stabilize from the beginning of the simulation, the total number of diffusion events, and the average number of steps an adatom takes to attach to an island or to nucleate. We emphasize on one case relevant to our results. When many islands or adatoms are present on the surface, adatoms that diffuse many times before attaching to an island or nucleating are on average nearer to their starting point than adatoms diffusing on a flat surface since most of those that diffused farther are already part of islands and do not contribute to the effective diffusion coefficient anymore. This results in an effective diffusion coefficient lower than the theoretical diffusion coefficient. Conversely, if most of adatoms that contribute to the effective diffusion coefficient diffuse few before attaching, the effective diffusion coefficient will come nearer to the theoretical diffusion coefficient.

In our KMC simulations, desorption, cluster diffusion, and concerted multiatomic events are not allowed. When an adatom arrives on the surface, it sticks to the arrival point. An adatom surrounded by four in-plane NNs is considered as immobile, and no overhangs are allowed. Process rates are computed according to the bond counting model of Eq. (3) with one of the previously defined aggregation modes, the MNR, when considered, as described by Eqs. (1) and (2) with $\varepsilon=1$, and the long jump model and path multiplicity as described by Eq. (4) and Fig. 1. The numerical parameters of the bond counting model are taken as $E_0=0.2$ eV, $E_\ell=0.3$ eV, $E_\uparrow=E_{\mathrm{ES}}=0.2$ eV, and $E_\Delta=0.05$ eV, which are typical experimental activation energies for metals [11,15,33–35]. That is, we are modeling metal homoepitaxy for simplicity reasons, although heteroepitaxy might lead to a lower surface friction needed for frequent long jumps. For this reason, we show in Appendix B that the activation energies can be shifted without changing the global trends.

In order to compare simulations that apply the MNR with others that do not, we need to fix a simulation parameter (other than the flux and the total coverage) that will be the same in every simulation. Since the most frequent process in the MNR simulations we performed is the free diffusion one ($n_i=n_f=n_\uparrow=n_\downarrow=0$ and $\ell=1$), we gave an equivalent prefactor to this process in all simulations. That is, for a same simulation temperature, the rate of the free diffusion process will always be the same whether the MNR applies or not. When the MNR does not apply, the prefactor in Eq. (1) does not depend on the activation energy and the common prefactor of all processes is therefore $\Gamma_0=\Gamma_{00}e^{-E_\ell/k_BT_{\mathrm{iso}}}$.

We set $\Gamma_{00}=10^5\ \mathrm{s}^{-1}$ to cover many orders of magnitude in the range of prefactors when the MNR applies, as can be observed in many systems [4]. Moreover, T_{iso} is fixed to 348.13 K. We recall the conditions that warrant that the MNR applies according to the MEE model: the activation energies are much larger than (i) k_BT_{iso}, and (ii) k_BT. Moreover, the MNR often fails above T_{iso} [4] so that we set $T < T_{\mathrm{iso}}$. To fulfill those conditions, the highest simulation temperature is fixed to $T_{\mathrm{max}}=280$ K. This also ensures that the isokinetic temperature is near the experimental range as frequently observed [4].

We draw the reader's attention to the fact that the value of T_{iso} is somewhat arbitrary since few data are available in the literature. Moreover, our simulations are set for E_d/k_BT

TABLE I. Difference between finite and infinite long jump extent limits (ℓ_{max}) for the total number of jumps ($\delta_{\ell\leq\ell_{max}}$)and the diffusion coefficient ($\Upsilon_{\ell\leq\ell_{max}}$). These values are derived from Eqs. (8) and (10).

	$T=250$ K		$T=265$ K		$T=274$ K		$T=280$ K	
ℓ_{max}	$\delta_{\ell\leq\ell_{max}}$ (%)	$\Upsilon_{\ell\leq\ell_{max}}$ (%)	$\delta_{\ell\leq\ell_{max}}$ (%)	$\Upsilon_{\ell\leq\ell_{max}}$ (%)	$\delta_{\ell\leq\ell_{max}}$ (%)	$\Upsilon_{\ell\leq\ell_{max}}$ (%)	$\delta_{\ell\leq\ell_{max}}$ (%)	$\Upsilon_{\ell\leq\ell_{max}}$ (%)
1	5.84	9.56	12.65	20.19	19.16	29.84	24.78	37.74
2	0.27	1.13	1.27	4.86	2.95	10.31	4.98	16.12
3	0.01	0.09	0.12	0.83	0.42	2.66	0.93	5.35
4	0.00	0.01	0.01	0.12	0.06	0.58	0.17	1.51
5	0.00	0.00	0.00	0.01	0.01	0.11	0.03	0.39

$\geq E_d/k_BT_{max}=12.4$, while long jumps and other concerted motions should be non-negligible for $E_d/k_BT\lesssim 4$ [29]. However, as shown in Appendix B, our results can be transposed to almost any T_{iso} value without losing global trends. That is, the temperature values we used are not absolute and should always be considered relatively to T_{iso}. For instance, Appendix B shows that multiplying T_{iso} by 10 results in values of E_d/k_BT ranging from 3.4 to 4.9 that give the same surface morphology as those with $E_d/k_BT\geq 12.4$.

A complete KMC treatment would require a simulation of jump extents up to infinity. However, such a treatment is far from being computationally realistic. A cutoff must be made in the long jump extent limit. To do so, we recall that the highest simulated temperature is $T=280$ K. This allows us to give in Table I the relative difference between finite and infinite long jump extent limits on the number of jumps and the diffusion coefficient according to Eqs. (8) and (10). We clearly see that considering only single hops can lead to a significant underestimate of the overall diffusion coefficient, especially at higher temperatures. Table I also reveals that using a jump extent limit of four atomic units is sufficient to ensure that the total number of jumps and the overall diffusion coefficient are within 1.5% of their saturation values for an infinite extent limit for the temperatures considered in this study. We therefore limit the jump extent to four atomic units in our simulations.

IV. RESULTS

Throughout this section, we present island size distributions and average island sizes in the submonolayer regime to evaluate the impact of the aggregation mode, the long jumps, and the MNR. We do not make use of scaling laws of the form

$$n_{ad}\sim\theta^{1/(i+2)}\left(\frac{F}{D}\right)^{i/(i+2)}e^{E_c(i)/(i+2)k_BT},$$

where n_{ad} is the density of islands, i is the critical size of islands, and $E_c(i)$ is the cohesion energy of islands of size i, because such laws are relevant only if one of the two following conditions are fulfilled. First, the temperature is held constant, so that

$$n_{ad}\sim\left(\frac{F}{D}\right)^{i/(i+2)},$$

or second, the cohesive energy $E_c(i)$ is known so that

$$n_{ad}\sim\left(\frac{F}{D}\right)^{i/(i+2)}e^{E_c(i)/(i+2)k_BT}.$$

None of those conditions are fulfilled here and i is not fixed in our study, so we rely on the previously mentioned analysis methods.

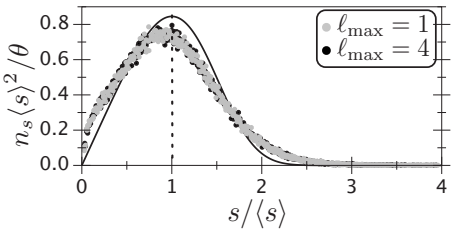

FIG. 2. Island size distributions for simulations with $\ell_{max}=1$ in the IA mode and $\ell_{max}=4$ in the RA mode. Data associated to temperatures of 250, 265, 274, and 280 K are shown. The data sets are averages of up to 100 simulations. The theoretical curve of Amar and Family [36] for the IA mode is shown as a solid line. A broken vertical line indicates the average value of the distribution ($s/\langle s\rangle=1$). The MNR is not considered.

A. Simulations without consideration of the MNR

We begin by comparing two sets of simulations that do not include the MNR. Figures 2 and 3 show the island size distributions ($n_s\langle s\rangle^2/\theta$ as a function of $s/\langle s\rangle$, where n_s is the density of islands of size s and $\langle s\rangle$ is the average island size) and the evolution of the average island size with temperature in the IA mode with $\ell_{max}=1$ and in the RA mode with $\ell_{max}=4$. All results of Fig. 2 are well described by the theoretical

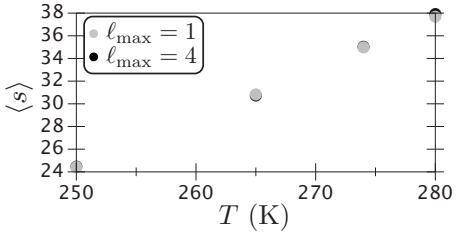

FIG. 3. Average size of islands for simulations with $\ell_{max}=1$ in the IA mode and $\ell_{max}=4$ in the RA mode. The MNR is not considered.

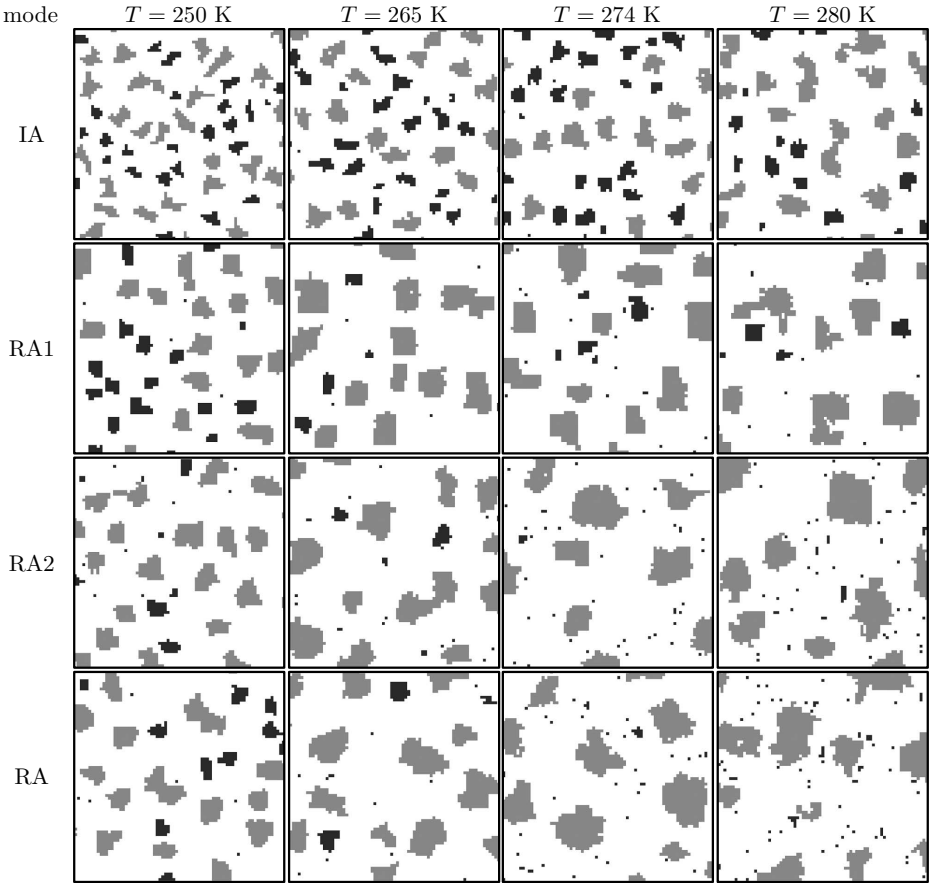

FIG. 4. Typical surface morphologies for various aggregation modes and $\ell_{\max}=1$. All islands with $s<\langle s\rangle$ are colored in black while others are illustrated in gray. Only a portion of size 75×75 of the original 250×250 simulated grid is illustrated. The MNR is considered.

curve (full line) of Amar and Family [36], developed for the IA mode.

Since the island size distributions and average island size are all superimposed in Figs. 2 and 3, no matter the aggregation mode or the extent limit, the detachment and long jump processes play no significant role on the shapes of the islands. This is due to the fact that detachment and long jump processes have low rates of less than 0.3 s^{-1} since the prefactor was fixed to a value of $\Gamma_0=2.203\times10^9$ s^{-1} to be coherent with simulations that consider the MNR (Sec. IV B). Hence, for the temperature range considered, $\max(D_{\ell\leq4}/D_{\ell=1})=\max(\nu_{\ell_{\max}\leq4})=1.000\,02$, where we apply Eqs. (9) and (A1) with $T_{\text{iso}}\to\infty$.

Therefore, we will apply the MNR for the rest of the paper, although it should always be kept in mind that simple relations involving temperatures and fluxes can be used to obtain similar results to those presented here even when the MNR does not apply (see Appendix B).

B. Simulations with consideration of the MNR

1. Impact of the aggregation mode

We now focus on the impact of aggregation for simulations that consider the MNR with $\ell_{\max}=1$. We obtain the typical surfaces shown in Fig. 4, where the black color is associated to islands with $s<\langle s\rangle$ (including adatoms), and the gray color is associated to other larger islands. For a given mode, we clearly see that the size of gray islands increases with temperature. While no visual distinction can be seen between the largest black islands and the smallest gray ones in the IA mode, this distinction becomes clearly apparent for the other modes from $T=265$ K. Indeed, increasing the temperature contributes to decreasing the size of the black islands while the gray islands increase in size. This trend is a clear signature of a bimodal island distribution which is enhanced when passing from one aggregation mode to the other (in the following order: IA, RA1, RA2, and RA). In order to quantify this bimodal behavior, Figs. 5 and 6 show the associated island size distributions and the average island size.

It is important to note that even if the specific representation of the bimodal distribution of Fig. 5 concentrates on the large islands, the distribution is fundamentally centered at $s/\langle s\rangle=1$ since

$$\frac{\sum_s sn_s\langle s\rangle^2/\theta}{\sum_s n_s\langle s\rangle^2/\theta}=\langle s\rangle.$$

The theoretical island size distribution of the IA model of Amar and Family [36] is illustrated by a solid line in Fig. 11 to highlight the impact of the aggregation mode on the island size distribution. While this model can describe relatively well the distributions of all modes at $T=250$ K and of the IA mode at any other temperature, it completely fails to describe the data points for Figs. 5(b)–5(d) in the RA1, RA2, and RA modes. For an increasing temperature (from (b) to (d)), the

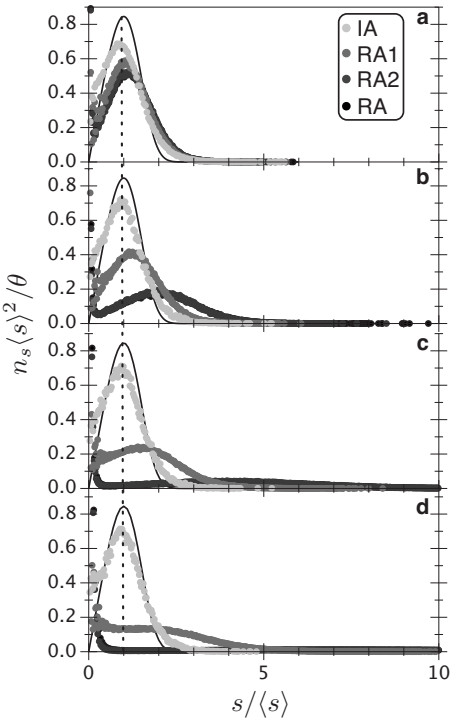

FIG. 5. Island size distributions for the four different aggregation modes (IA, RA1, RA2, and RA) for temperatures of (a) 250, (b) 265, (c) 274, and (d) 280 K. The data sets are averages of up to 2800 simulations. The theoretical curve of Amar and Family [36] for the IA mode is shown as a solid line. A broken vertical line indicates the average value of the distribution ($s/\langle s\rangle=1$). The MNR is considered.

size distributions associated with the different aggregation modes broaden, and become progressively separated from each other. This clearly shows that for those aggregation regimes, two growth modes are present, one for small islands and a second one for large islands.

Figure 6 emphasizes the bimodal island size distribution. Indeed, while the average size of islands increases with temperature for the IA mode, it decreases at a high temperature for every other mode. This tendency is enhanced when passing from the RA1 to the RA2 and then to the RA mode. On

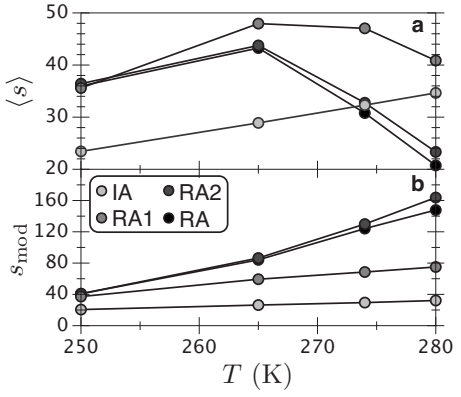

FIG. 6. (a) Average size of islands and (b) most frequent size of large islands for the IA, RA1, RA2, and RA modes. The MNR is considered.

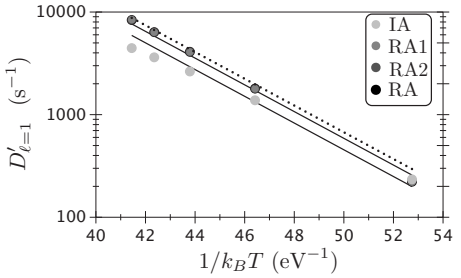

FIG. 7. Effective diffusion coefficient for the different aggregation modes when the MNR is considered. The data associated with RA1, RA2, and RA modes are essentially superimposed. The dotted line corresponds to the theoretical diffusion coefficient ($D_{\ell=1}=a^2\Gamma_{00}e^{-\alpha}$) and the two other full lines are fits of the equation $D'_{\ell=1}=Aa^2\Gamma_{00}e^{-\alpha}$ (see the text for more details).

the other hand, the most frequent size of large islands [37] (s_{mod}) increases monotonically with temperature for any mode.

The number, the size, and the shape of islands vary with temperature, in a way that differs significantly from one aggregation mode to the other. For instance, the island edges in Fig. 4 pass from rough to nearly flat and rough again when going from the IA to the RA1 modes, and then to the RA2 mode.

We computed the effective diffusion coefficient given by Eq. (12) and compared it with the theoretical diffusion coefficient ($D_{\ell=1}=a^2\Gamma_{00}e^{-\alpha}$), valid for single adatoms on a flat surface. We show in Fig. 7 results for all the aggregation modes (circle symbols). The dotted line is the theoretical diffusion coefficient and the full lines are found by fitting A in the equation $\ln D'_{\ell=1}=\ln(Aa^2\Gamma_{00})-\alpha$ with the least mean square method. Only two fitted lines are visible on Fig. 7 since all data points of RA1, RA2, and RA modes are essentially superimposed. While the Arrhenius behavior of the effective diffusion coefficient is quite clear when we compare the dotted line with data sets, we note some discrepancies between data sets and fitted lines. Indeed, for the IA mode, the effective diffusion coefficient tends to lie lower than the fitted line as the temperature increases, whereas we observe the opposite behavior for all other modes. For the IA mode, the adatoms that remain near their starting point of diffusion contribute to lower $D'_{\ell=1}$ and this phenomenon gets more important as the temperature increases. For all other modes, the high number of adatoms newly detached from an island that can reattach in few steps compensate the effect observed for the IA mode. As the temperature increases, the number of adatoms increases. This explains why the effective diffusion coefficient lies higher than the fitted lines for the RA1, RA2, and RA modes.

2. Impact of long jumps

Table I shows that even when long jumps appear negligible with respect to single hop ($\delta_{\ell\leq\ell_{\max}}$parameter), the impact on the diffusion coefficient can be significant ($\Upsilon_{\ell\leq\ell_{\max}}$parameter). Indeed, since a long straightforward jump of extent ℓ travels a distance that can only be achieved by the relatively rare case when ℓ single successive hops all

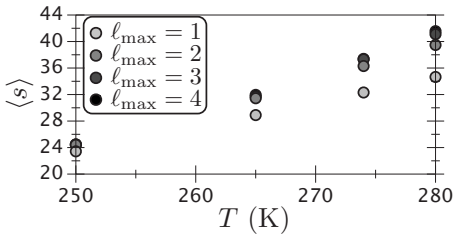

FIG. 8. Average size of islands in the IA mode for long jump extent limits from 1 to 4. The MNR is considered.

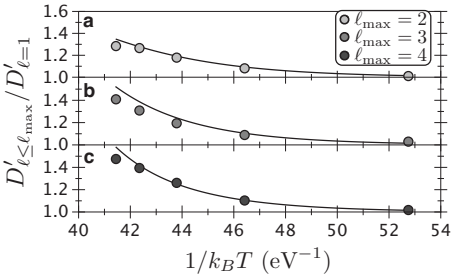

FIG. 9. Relative effective diffusion coefficient with respect to the value found when $\ell_{max}=1$ for the IA mode when the MNR is considered. The prime symbol on $D'_{\ell\leq\ell_{max}}$ is used to distinguish the effective diffusion coefficient from the theoretical one. The fitted lines show $\nu_{\ell\leq\ell_{max}}$. An effective diffusion coefficient with an Arrhenius behavior would have a constant value of $D'_{\ell\leq\ell_{max}}/D'_{\ell=1}=1$.

occur in the forward direction, its contribution on the diffusion coefficient is significant. Therefore, $\Upsilon_{\ell\leq\ell_{max}}$ gives a better indication than $\delta_{\ell\leq\ell_{max}}$ on the impact of long jumps on surface morphologies.

When the MNR applies and long jumps are possible in the IA mode, the island size distributions are superimposed, and are relatively well described by the theoretical curves of Amar and Family [36]. The average island size (Fig. 8) increases with the temperature and the long jump extent limit. At $T=250$ K, the average island sizes are almost equal for every long jump extent limit. This is consistent with Table I, where we see that, at $T=250$ K, increasing the long jump extent limit induces only small changes on an already low $\Upsilon_{\ell\leq\ell_{max}}$. At higher temperatures, the variations on $\Upsilon_{\ell\leq\ell_{max}}$ for various long jump extent limits are more important. This is responsible for the differences in the average island sizes at a given temperature on Fig. 8. We see that for the highest simulated temperature ($T=280$ K), $\ell_{max}=4$ is largely sufficient to describe the surface topography evolution since the contribution of long jumps has an asymptotic behavior with the jump extent limit. This confirms the choice of the cutoff performed in the long jump extent limit in our KMC simulations.

While the island size distributions are all superimposed as is the case for simulations that do not apply the MNR, the average size changes significantly when the long jump extent limit increases. This is due to the increase in the diffusion coefficient. We computed the effective diffusion coefficient for various jump extent limits and normalized it by $D'_{\ell=1}$ as given in Fig. 7. This normalization allows one to compare directly $D'_{\ell\leq\ell_{max}}/D'_{\ell=1}$ with $\nu_{\ell\leq\ell_{max}}$ (full lines) and clearly identifies supra-Arrhenius behaviors for the effective diffusion coefficients as predicted by Eqs. (9) and (A1). This result emphasizes the fact that long jumps become more important with increasing the temperature. This trend is also supported by the values reported in Table I. The factor responsible for the data points lying lower than $\nu_{\ell\leq\ell_{max}}$ in Fig. 7 is responsible for the equivalent behavior in Fig. 9.

3. Combined impact of the reversible aggregation mode and long jumps

From now on, only the RA mode will be simulated since we want to study the impact of aggregation reversibility combined to long jumps. Up to now, results indicate that the global impact of the aggregation reversibility is to create a bimodal island size distribution that spreads out as the temperature increases. Moreover, the diffusion coefficient increases with long jumps and results in a larger average island size. We therefore want to investigate what happens when aggregation reversibility and long jumps are considered in a same KMC simulation.

When we study the impact on the effective diffusion coefficient, we obtain essentially the same results as shown in Fig. 9. In fact, the agreement of theoretical and experimental curves is even better when long jumps and aggregation reversibility are combined. This is due to the increased number of detached adatoms that only need few diffusion steps to reattach. The contribution of those adatoms counterbalances the adatoms that stay near their starting point of diffusion and gives an effective diffusion coefficient near the prediction of Eqs. (9) and (A1). This clearly indicates that for $\ell_{max}>1$, the diffusion coefficient has a supra-Arrhenius behavior.

We now concentrate on the temperature range for which the contribution of long jumps to the diffusion coefficient is the most important. Typical surface morphologies are presented in Fig. 10 where the black color is associated to islands with $s<\langle s \rangle$ (including adatoms), and gray is associated to other larger islands. Starting from $T=250$ K and $\ell_{max}=1$, we clearly see that black islands get smaller while gray islands get larger as the temperature or the jump extent limits increase. Again, this is characteristic of a bimodal distribution and the island size distributions of Fig. 11 can be used to quantify this behavior. The vertical broken line in Fig. 11 identifies the average point for all distributions ($s/\langle s \rangle$) and illustrates how the distributions spread out. We can compare the results obtained in Fig. 5 in which $\ell_{max}=1$ and the aggregation mode was variable with results presented in Fig. 11. Indeed, the broadest distributions in Fig. 5 are the narrowest distributions in Fig. 11. We draw the reader's attention to the fact that the curves associated to $\ell_{max}=1$ in Fig. 11 are identical to the RA curves of Fig. 5 although the data are presented on a different scale in order to focus on the large island mode. We show in Appendix C that synergistic effects are observed between the reversible aggregation mode and long jumps.

Figure 12 presents a close-up of the island size distribution for $\ell_{max}\leq 4$ in order to emphasize the growth of small islands (note the relative scale used in Figs. 11 and 12). As

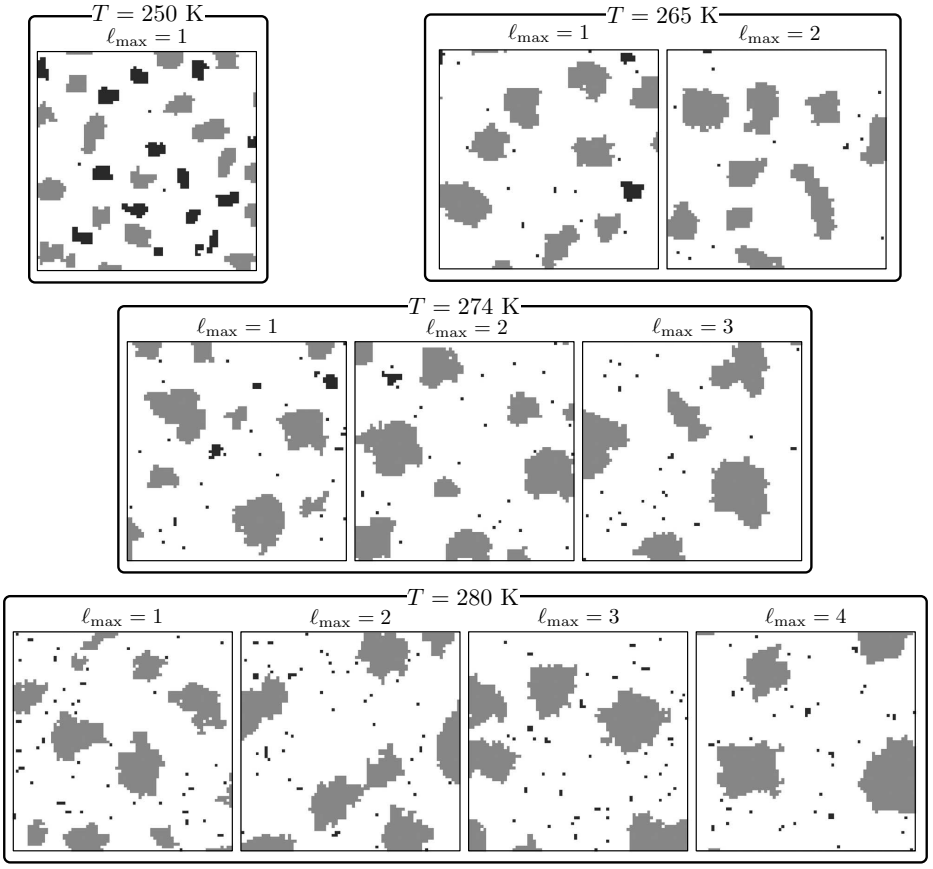

FIG. 10. Typical surface morphologies obtained for several extent limits ($\ell_{max}=1,2,3,4$) at $T=250$, 265, 274, and 280 K. All islands with $s<\langle s\rangle$ are black while the others are gray. For clarity, only a portion (75×75) of the original 250×250 simulated grid is shown. The MNR is considered.

the temperature increases, the small island density increases (see Fig. 12). This results in a decrease of the average size of stable islands $\langle s_c\rangle$ (such that $s\geq2$) [38] (see Fig. 13). Indeed, this figure reveals that the average size of stable islands has a nonmonotonically increasing behavior with increasing temperatures. In Fig. 13, $\langle s_c\rangle$ is used instead of $\langle s\rangle$ because the latter is so much influenced by the adatom density that values are nearly superimposed for all jump extent limits. We mention briefly that we do not present the s_{mod} values because their precise numerical determination requires one to average a very large number of simulations, and because they reproduce essentially the results of Fig. 6(b). That is, the most frequent size of large islands increases with temperature.

We see in Figs. 11 and 13 that for simulations that combine long jumps and the RA mode, the cutoff performed on the jump extent limit (that is, $\ell_{max}\leq4$) is justified because of the observed asymptotic behavior.

Since the jump extent limit can have a major impact on the island size distribution, we have tried to compensate such an effect by modifying the temperature. Hence, we have fixed the effective diffusion coefficient to its maximal value when $\ell_{max}=1$, that is, $D'=8300a^2/s$. To obtain this constant diffusion coefficient, temperatures of 280.0 K, 274.5 K, 273.1 K, and 272.8 K were used for jump extent limits going from 1 to 4, respectively. The resulting evolution of the average island size, and adatom and island densities are presented in Fig. 14, and the associated surface morphologies are shown in Fig. 15. First, Fig. 14 shows significant density shifts within the different jump extent limits considered, an asymptotical convergence being observed for large ℓ_{max} values. We see that the data points for $\ell_{max}=4$ essentially reproduce the results obtained with $\ell_{max}=3$. For a fixed value of the equivalent diffusion coefficient, the following features are observed as the jump extent limit decreases.

(1) The coalescence is retarded because the attachment and detachment kinetics favors the formation of new small islands from coalesced islands, and this compensates at least partially the coalescence [Fig. 14(a)].

(2) The adatom density increases more rapidly and stays higher, which indicates the importance of the attachment and detachment kinetics as the temperature increases [Fig. 14(a)].

(3) The island densities (for $s\geq2$) increase more rapidly and remain higher, which is due to the important adatom density that can form small islands [Fig. 14(a)].

(4) The average size of stable islands, $\langle s_c\rangle$, is lower because of the higher island density [Fig. 14(b)].

(5) Each branch of the bimodal distribution becomes narrower (Fig. 15); that is, small islands become larger and large islands become smaller.

These results are due to the fact that the diffusion coefficient itself is insufficient to explain the surface morphologies observed. Indeed, the temperature is really important because a small change of temperature can induce a major change in the relative rate of the different events, in particular, detachment events here.

V. DISCUSSION

In this section, we concentrate on three main consequences of considering a contribution from long jumps or the

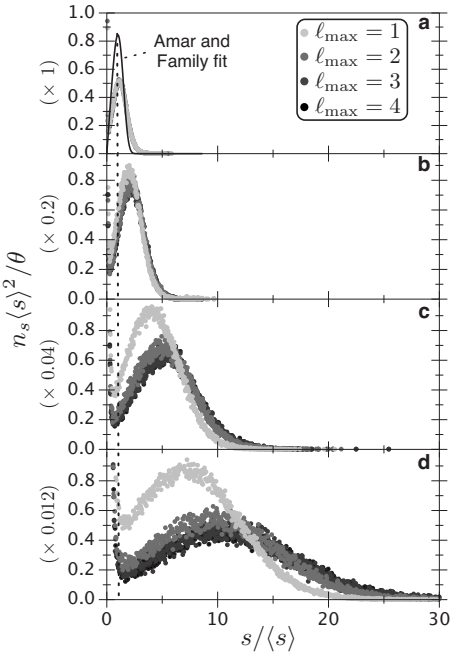

FIG. 11. Island size distribution for $\ell_{max} \leq 4$ and temperatures of (a) 250 K, (b) 265 K, (c) 274 K, and (d) 280 K. These figures were scaled to emphasize the large island mode. The scaling factor is indicated in parentheses at the left of each subplot. A broken vertical line indicates the average value of the distribution ($s/\langle s\rangle = 1$). A maximum of 7000 simulations were performed for each temperature and the figures show the average distribution. The theoretical curve of Amar and Family [36] for the IA mode is only shown in (a) because it does not apply well to other data sets. The MNR is considered.

reversible aggregation mode, whether the MNR applies or not: (i) a supra-Arrhenius diffusion coefficient, (ii) a bimodal island size distribution, and (iii) the corresponding island morphologies.

A. Supra-Arrhenius diffusion coefficient

We observed in Fig. 9 that the supra-Arrhenius trend predicted for the diffusion coefficient of single adatoms diffusing on a flat surface can also describe rather well the submonolayer growth regime.

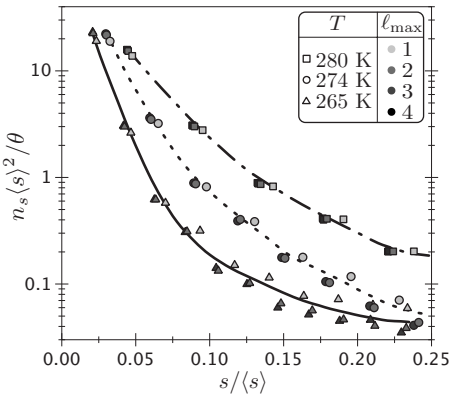

FIG. 12. Close-up on the small island mode [size below $0.25\langle s\rangle$] of the island size distribution for $\ell_{max} \leq 4$. The fitted curves are only guidelines. The MNR is considered.

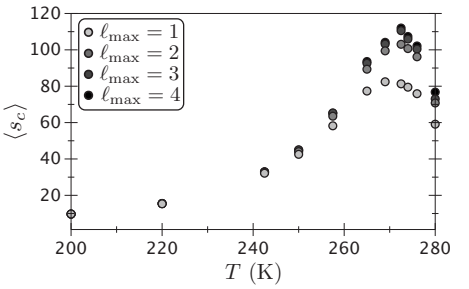

FIG. 13. Average stable island size evolution with temperature for $\ell_{max} \leq 4$. Only islands with $s \geq 2$ are considered. The MNR is considered.

To verify this, we used the effective diffusion coefficient as described by Eq. (12). While this parameter depends on many factors such as the compactness and average size of islands, the time the simulation time step takes to stabilize from the beginning of the simulation, the total number of diffusion events, and the average number of steps an adatom takes to attach to an island or to nucleate, it still provides a reliable way to compare the diffusion coefficient in simulations with similar temperatures and adatom densities. Thus, even though the effective diffusion coefficient in Fig. 7 does

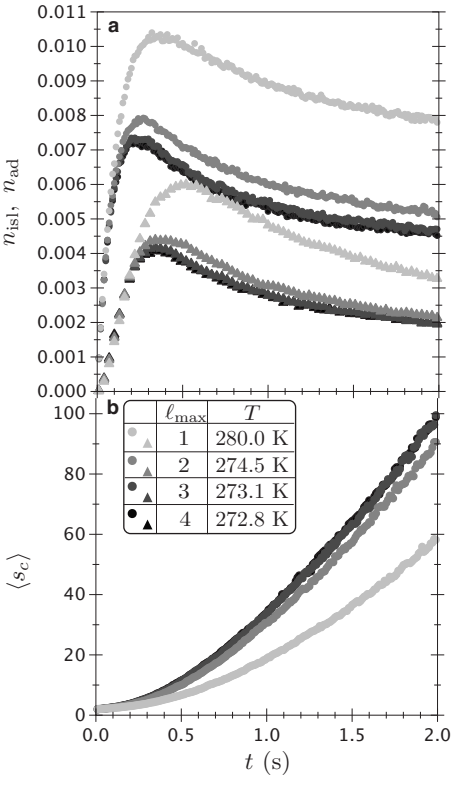

FIG. 14. Evolution (as a function of t, the simulation time) of adatom density [circles in (a)], island density [triangles in (a)], and average size of stable islands with $s \geq 2$ [(b)] for a fixed value of the effective diffusion coefficient ($D' = 8300a^2/\mathrm{s}$, the highest value obtained when $\ell_{max} = 1$). The data points are averaged over 30 simulations for each set. The MNR is considered.

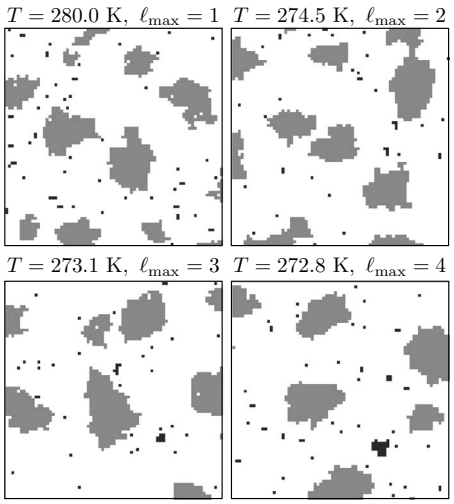

FIG. 15. Typical surface morphologies for a constant diffusion coefficient $D=8300a^2/\mathrm{s}$. All islands with $s<\langle s\rangle$ are colored in black while others are illustrated in gray. Only a portion of size 75×75 of the original 250×250 simulated grid is illustrated. The MNR is considered.

not exactly have an Arrhenius behavior, the value of $D'_{\ell\leq\ell_{\max}}/D'_{\ell=1}$ is almost identical to the theoretical $\nu_{\ell\leq\ell_{\max}}$ values in Fig. 9.

According to our model, a supra-Arrhenius diffusion coefficient behavior should be observed every time long jumps are present, at least in the submonolayer regime. This effect is even stronger when the MNR is taken into account. As indicated previously, the Arrhenius form of the rate of activation of the diffusion process is derived from an harmonic approximation from the TST. Thus other phenomena such as multiatomic concerted motions or anharmonic effects may also modify the Arrhenius behavior, especially at high temperature [39]. Thermal expansion [34] and finite-barrier corrections [40] have also been shown to affect the rate of activation of diffusion events and thus the Arrhenius behavior of the diffusion coefficient. Finally, memory effects, related either to an insufficient time of relaxation of the surface during the diffusion of particles or to the influence of other particles on the surface might also result in deviation from the Arrhenius behavior [29].

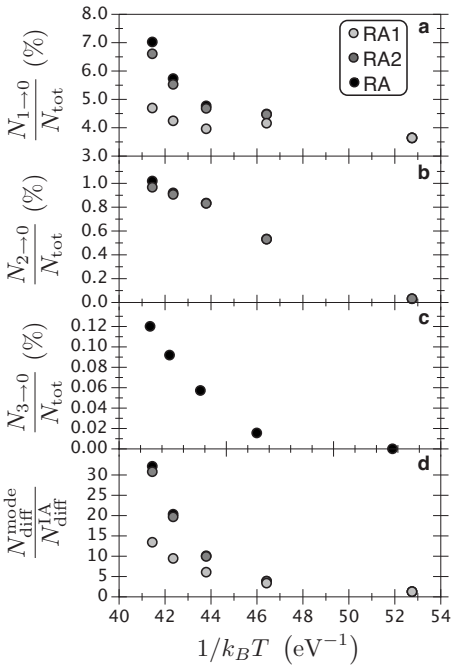

FIG. 16. [(a)–(c)] Weight of detachment events ($N_{n_i\to n_f}$) with respect to the total number of events (N_{tot}) throughout the whole simulation for RA1, RA2, and RA modes. (d) Ratio between the number of free diffusion events ($n_i=n_f=n_\uparrow=n_\downarrow=0$) of RA1, RA2, and RA modes, and the IA mode.

Nevertheless, few experimental evidences clearly show such supra-Arrhenius behavior. This could simply be related to the fact that experimental uncertainties are large enough for an Arrhenius relation to correctly describe the data points even though the best fit would be a supra-Arrhenius behavior. This is supported by the theoretical results of Boisvert and Lewis [12] that predict a supra-Arrhenius behavior as well. Such a behavior in the evolution of the diffusion coefficient with temperature leads to a faster increase in the size of large islands than when an Arrhenius behavior is present. The layer-by-layer transition should then appear at a lower temperature.

At its most ($T=280$ K), the supra-Arrhenius behavior we predict is 61% higher than what a model that forbids long jump would give since $D_{\ell<\infty}/D_{\ell=1}=\nu_{\ell<\infty}=1.61$. To achieve a 61% uncertainty on $D_{\ell=1}$, E_ℓ or Γ_{00} should have uncertainties of 19% or 61%, respectively. Even though those uncertainties are relatively small compared to some experimental uncertainties, the theoretical supra-Arrhenius behavior remains. We also believe that understanding the impact of long jumps on the diffusion coefficient is important enough to discard multiatomic concerted events, anharmonic effects, thermal expansion, finite-barrier corrections, and memory effects that could affect the Arrhenius behavior.

B. Bimodal island size distribution

In the IA mode or when detachment events are not frequent (as we saw in Fig. 2 with the conditions we used when the MNR does not apply), the island size distribution is clearly unimodal as predicted by the theoretical model of Amar and Family [36]. However, as soon as the detachment events become important, the island size distribution becomes bimodal. Still, at a temperature of 250 K, the distinction between the size of islands above and below the average size is difficult at any aggregation mode (as we saw in Fig. 4) because one of the island size distribution modes is almost centered on $s=\langle s\rangle$ (see Fig. 5). The distribution spreads out as atoms surrounded by a greater number of NNs are allowed to detach and the temperature increases. When atoms are allowed to detach, they can leave low coordination sites to attach to higher ones. This explains why the most frequent size of large islands in Fig. 6(b) increases when going from the IA to the RA2 modes. For the RA mode, we obtain a s_{mod} lower than that for the RA2 mode. However, we do not know if this result is due to the imprecision in the technique used to find the most frequent size of large islands. The average

island size is a more precise value and has a somewhat different behavior. Indeed, as soon as atoms can detach from islands, $\langle s \rangle$ is no longer monotonically increasing with temperature as shown in Fig. 6(a). Moreover, as atoms can detach from higher coordination sites, the average island size decreases more rapidly with increasing temperatures.

To understand the behavior of s_{mod} and $\langle s \rangle$, we show, in Figs. 16(a)–16(c), the relative number of detachment events ($N_{n_i \to 0}$, where the subscript indicates that events such that the initial and final number of in-plane NNs are n_i and 0 are performed) with respect to the total number of events throughout a simulation (N_{tot}). In the RA mode, n_i can range from 1 to 3 for detachment events. For the RA1 (RA2) mode, this value can only take the value 1 (can range from 1 to 2), and for the IA mode, no detachment events are possible. In Fig. 16(d), we show the number of diffusion events of all aggregation modes with respect to the number of diffusion events of the IA mode.

We see that even $N_{1 \to 0}/N_{\mathrm{tot}}$ increases when going from the IA to the RA mode. Indeed, adatoms surrounded by more than one in-plane NN that detach from an island potentially leave more atoms surrounded by only one in-plane NN in the island edge, which explains the increase in $N_{1 \to 0}/N_{\mathrm{tot}}$. Increasing $\Sigma_{n_i} N_{n_i \to 0}/N_{\mathrm{tot}}$ is responsible for an increase of the adatom density, and therefore the island density. The global impact is to lower the average island size.

Moreover, as a greater number of atoms detach, the number of diffusion events can increase significantly. For instance, the number of diffusion events at $T=280$ K is more than 30 (12) times more important in the RA and RA2 modes (RA1 mode) than it is in the IA mode [see Fig. 16(d)]. This enhanced number of random walk steps allows adatoms to find more stable sites and explains the increased value of s_{mod} as adatoms can detach from higher coordination sites.

Similarly, when long jumps are allowed, the diffusion coefficient increases and the size of large islands is expected to increase. This results in a broader island size distribution (see Fig. 11), where the broadest distribution in each of Figs. 5(a)–5(d) subfigures is exactly the same as the narrowest in Figs. 11(a)–11(d) subfigures. As the temperature increases, the detachment of adatoms from islands increases and the small island mode becomes more important (see Fig. 12). In this sense, the small island mode emerges from the large island one. Thus, the island size distributions spread and become strongly bimodal [see Fig. 11(b)–11(d) scaled to emphasize the large island mode]. We show in Appendix C that synergistic effects are found between the RA mode and long jumps. Above 250 K, the most important mode, illustrated in Fig. 12, is centered on small islands even though small islands form and fragment frequently enough to be considered metastable. Moreover, while the mode associated with larger islands is the smallest, most of the atoms are in large islands. Nevertheless, some temperatures should exist at which this small islands mode would be the less representative of the distribution, and where coarsening would be very important.

We now need to compare our finding of a bimodal island size distribution with the distributions reported in the literature. Bimodal distributions have already been claimed in the presence of (i) cluster diffusion [41], (ii) adatom exchange with a surface atom [42], and (iii) thermodynamic equilibrium in a strained system [43]. The (i) bimodal distribution obtained by Kuipers and Palmer [41] is due to the increase in the island mobility with respect to adatom mobility. This higher mobility lowers the number of islands, and small islands (including adatoms) are less likely to find a larger one to attach to. The bimodal distribution (ii) observed by Zangwill and Kaxiras [42] arises from the increase in stable nuclei after an exchange process between an adatom and a substrate atom. Finally, the distribution (iii) was obtained by Meixner *et al.* [43] from a KMC simulation of self-organized growth in strained systems. In their simulations, the system was allowed to reach a thermodynamic equilibrium after deposition where kinetic processes are dominating. During initial kinetic steps, the island size increases with temperature because a high temperature favors the diffusion and the adatoms reach existing islands much more frequently than they nucleate into new islands. Then, when the system evolves to reach a thermodynamic equilibrium, entropy favors the island sizes that decrease with the temperature. An additional study, considering reversible aggregation [13], resulted in a bimodal distribution. Although the authors did not mention explicitly a bimodal island size distribution, they admitted that the data associated to small islands did not collapse on the island size distribution scaling curve. Their distribution is much narrower than those shown in Fig. 11. The set of activation energies and the low temperature (compared to those activation energies) used in their study is sufficient to explain this difference. In every way, the bimodal distributions we obtained are much more pronounced than the distributions described above.

We want to emphasize that while we do not explicitly allow the surface to reach a thermodynamic equilibrium in our simulations, an analysis of a given process event rate at high temperature reveals that the probability of performing an event associated to a process with $(n_i, n_f, \ell, n_\uparrow, n_\downarrow)$ is practically the same as performing one of a process with $(n_f, n_i, \ell, n_\uparrow, n_\downarrow)$ during the whole simulation. That is, the surface arranges rapidly in such a way that the number of possible events for a given process multiplied by its rate is approximately equal to the number events of the reverse process times the rate of this process. Thus, at high temperature (around 250 K and above) our system reaches a quasiequilibrium state during growth. However, unlike the results of Meixner *et al.* [43], our island size distribution spreads out with increasing temperature. This fundamental difference is due to the causes of the bimodal island size distribution. Indeed, the KMC results of Meixner *et al.* are due to a competition between cohesion and strained energy while our results are due to a competition between attachment and detachment of adatoms. This quasiequilibrium state leads to a coarsening process that is almost inexistent. On average, adatoms attach to large islands at the same rate they detach and the same is true for small islands.

C. Island morphology

The attachment and detachment kinetics have a strong impact on the morphologies of islands in the bimodal distribution. Indeed, the edge roughness varies a lot from one

aggregation mode to the other (see Fig. 4). In the RA1 mode, when only atoms surrounded by one in-plane NN can detach, the island edges are almost flat, even at 280 K. Thus, the edge diffusion and the detachment of low coordination number atoms both contribute to decrease the roughness of islands. In the IA mode, as soon as an adatom reaches an island, it sticks to it and only edge diffusion can contribute to flatten the island edges. In the RA2 mode, the edge diffusion contributes to lower the island edge roughness, but the detachment of atoms surrounded by two in-plane NNs counterbalances this behavior. The island edge roughness is even more important in the RA mode since more atoms can detach from islands. Hence, the RA1 mode leads naturally to the flattest island edges. Conversely, the IA at low temperature and the RA at high temperature lead to the roughest island edges.

Similarly, the island edge roughness increases with temperature since the rate of detachment events increases (see Figs. 4 and 10). This process is, however, stabilized by the large number of attachment sites and the attachment and detachment equilibrium that occurs. When the detachment from small islands is important, the attachment cannot compensate and the islands are generally broken apart to form small metastable islands. This is a direct consequence of the bond counting model for which the detachment of an atom becomes more difficult when the number of in-plane NNs is large. The atoms that are the most likely to detach from islands are those with only one in-plane NN. Indeed, we observe that when detachment is possible, the islands containing atoms attached by only one edge are less stable than others. This can be confirmed by oscillations in the island size distributions of small islands which are not monotonically decreasing.

We showed in Figs. 14 and 15 that the diffusion coefficient alone is insufficient to predict the surface and island morphologies. This is due to the fact that the events associated with each process are performed with a different relative probability at different temperatures, independently of the diffusion coefficient. Indeed, the diffusion coefficient is a function of the process rates but not the reverse. As the long jump extent limit increases, the diffusion coefficient increases but the detachment frequency remains essentially constant. Hence, as $\ell_{\max}$ increases, islands become larger while maintaining a similar edge roughness. In brief, the island size depends on the temperature and $\ell_{\max}$, while the island roughness is mostly a function of the temperature. As revealed in Fig. 13 for stable islands, the observed bimodal distribution is responsible for a nonmonotonic increase of the average island size. This evolution presents a maximum near the point where the increasing diffusion coefficient is still able to compensate for the detachment of adatoms from island edges.

VI. SUMMARY AND CONCLUDING REMARKS

We have considered the impact of long jumps and reversible aggregation on a simple cubic (100) surface growth when process rates are subject to compensation effects. We compared our theoretical results for a single adatom diffusing on a flat surface with KMC results for more complex surfaces involving many adatoms and islands in the submonolayer regime. We found that there is a great agreement between our theoretical and KMC results for the supra-Arrhenius behavior of the diffusion coefficient. Our KMC simulations also show a clear bimodal island size distribution at high temperatures or long jump extent limits. In this bimodal distribution, the most important mode is the small island's one, while most of the atoms are in large islands. This is due to the competition between the increasing diffusion coefficient that favors large islands and the raising rate of detachment of atoms from islands, which favors small islands. At the same time, adatom attachment and detachment processes are responsible, as the temperature increases, for the large island's edge roughness and the metastability of small islands.

We have restricted our studies to the effect of long jumps and detachment processes on island sizes and morphology evolutions. However, other diffusion events with a high activation energy could have an important impact on island evolution, especially when the MNR applies. For instance, cluster and vacancy diffusion should be considered. Indeed, studying the surface Cu(100) with *ab initio* static relaxation methods and semiempirical molecular-dynamics simulations, Boisvert and Lewis have found that some compensation effects were observed for adatoms, dimers, and vacancy self-diffusion, and that the same MNR parameters (Γ_{00} and T_{iso}) could describe the compensation observed for all those processes [44]. In the same way, compensation effects have been observed in many more cases of cluster diffusion [45,46]. Moreover, many surfaces for which Boisvert and Lewis have shown clear compensation effects [2] also present cluster diffusion barriers of the same order of magnitude as adatom diffusion energies [47] that could benefit from additional compensation effects related to the number of atoms involved in the concerted motion [21].

While our results were obtained for an explicit application of the MNR, we emphasize the fact that a supra-Arrhenius diffusion coefficient behavior and a bimodal distribution with the island morphologies presented earlier are to be seen for every surface with significant long jump rates and attachment and detachment kinetics, whether compensation effects are observed or not.

ACKNOWLEDGMENTS

This work was funded by Le Fonds québécois de la recherche sur la nature et les technologies (FQRNT) of Québec and the Ministère du développement économique, de l'innovation et de l'exportation (MDEIE) of Québec. Computational facilities have been kindly provided by the Réseau québécois de calcul de haute performance (RQCHP). We are thankful to P. Kratzer for the initial version of the KMC code and to A. Yelon for valuable discussion on the Meyer-Neldel rule.

APPENDIX A: DIFFUSION COEFFICIENT FOR LONG JUMPS

To compute the statistical distance that an adatom can travel with respect to time, we start by assuming that the

time step between each of its diffusion events is constant on a flat isotropic surface with zero flux. We can thus write the diffusion coefficient with respect to the number of diffusion events. After N diffusion steps, a single adatom located at the grid point (i,j) with respect to the starting point of diffusion $(0,0)$ will statistically be at a squared distance

$$d^2_{\ell\le\ell_{\max}}(i,j) = 4a^2 \sum_{\ell=1}^{\ell_{\max}} p_\ell \sum_{m=0}^{\ell-1} \binom{\ell}{m} (i^2 + j^2 + m^2 + [\ell - m]^2)$$
$$= a^2(i^2 + j^2) + \nu_{\ell\le\ell_{\max}},$$

with

$$\nu_{\ell\le\ell_{\max}} = \frac{a^2 e^{\alpha}(1-e^{-\alpha})(1-2e^{-\alpha})}{2(1-e^{-\alpha\ell_{\max}}[2^{\ell_{\max}+1}\{1-e^{-\alpha}\} - \{1-2e^{-\alpha}\}])} \times \sum_{\ell=1}^{\ell_{\max}} \frac{2^\ell(\ell^2+\ell) - 2\ell^2}{e^{\alpha\ell}}. \quad \text{(A1)}$$

We note $n_N = n_N(i,j)$ the probability of an adatom to be located at a grid point (i,j) after N diffusion events. Naturally, if we sum over all sites, $\Sigma_{i,j} n_N(i,j) = 1$. Therefore, the average squared distance of diffusion after N time steps is

$$\langle R^2(N)\rangle = \frac{\sum_{i,j} n_N a^2(i^2+j^2)}{\sum_{i,j} n_N}$$
$$= \sum_{i,j} n_N a^2(i^2+j^2)$$
$$= \sum_{i,j} n_{N-1} d^2_{\ell\le\ell_{\max}}(i,j)$$
$$= \sum_{i,j} n_{N-1}(a^2[i^2+j^2] + \nu_{\ell\le\ell_{\max}})$$
$$= \sum_{i,j} n_{N-1} a^2(i^2+j^2) + \nu_{\ell\le\ell_{\max}}$$
$$= \sum_{i,j} n_{N-2} a^2(i^2+j^2) + 2\nu_{\ell\le\ell_{\max}}$$
$$= \sum_{i,j} n_0 a^2(i^2+j^2) + N\nu_{\ell\le\ell_{\max}}. \quad \text{(A2)}$$

The previous sums are made over all i and j grid points of the surface. However, because many sites are out of range after a finite number of steps, many $n_N(i,j)$ are equal to zero. Since we began this demonstration by assuming that a single adatom was located at the grid point $(0,0)$, $\Sigma_{i,j} n_0(i,j) a^2(i^2+j^2) = 0$. Consequently, we find, by recurrence,

$$\langle R^2(N)\rangle = N\nu_{\ell\le\ell_{\max}}.$$

Thus, $\langle R^2(N)\rangle/N$ is constant if the temperature and the jump extent limit $\ell_{\max}$ are fixed. We give below some results for Eq. (A1).

$$\nu_{\ell=1} = a^2, \quad \text{(A3)}$$

$$\nu_{\ell\le2} = a^2\left(\frac{1+8e^{-\alpha}}{1+3e^{-\alpha}}\right), \quad \text{(A4)}$$

$$\nu_{\ell\le3} = a^2\left(\frac{1+8e^{-\alpha}+39e^{-2\alpha}}{1+3e^{-\alpha}+7e^{-2\alpha}}\right), \quad \text{(A5)}$$

$$\nu_{\ell\le4} = a^2\left(\frac{1+8e^{-\alpha}+39e^{-2\alpha}+144e^{-3\alpha}}{1+3e^{-\alpha}+7e^{-2\alpha}+15e^{-3\alpha}}\right) \quad \text{(A6)}$$

$$\nu_{\ell<\infty} = a^2\left(\frac{1-e^{-\alpha}-6e^{-3\alpha}+8e^{-4\alpha}}{[1-e^{-\alpha}]^2[1-2e^{-\alpha}]^2}\right),$$
$$\text{valid only if } \alpha > \ln(2). \quad \text{(A7)}$$

We briefly mention that if we take the limit $\alpha \to -\infty$ in the equations above, except Eq. (A7) which does not allow this condition, we obtain $\nu_{\ell=\ell_{\max}}$, that is, when only jumps of the maximum extent are allowed.

From the Einstein equation, we can find the diffusion coefficient, remembering that the jump extent is not strictly equivalent to the jump length,

$$D_{\ell\le\ell_{\max}} = \lim_{t\to\infty}\frac{\langle R(t)^2\rangle}{vt} = \lim_{N\to\infty}\frac{N\nu_{\ell\le\ell_{\max}}}{vN\tau} = \frac{\nu_{\ell\le\ell_{\max}}}{v\tau}, \quad \text{(A8)}$$

where τ is the uniform time between each diffusion step. In our KMC simulations, diffusion events are modeled as Poisson processes. Therefore, the diffusion time step is not constant. Substituting the average time step $\langle\Delta t\rangle$ to τ in Eq. (A8) we can have an approximation of the diffusion coefficient for which the precision will increase with the number N of steps considered.

As established in Eq. (11), we can find the diffusion time step, noting that $\mathbf{R}(t) = \Sigma_i \Gamma_i$ since there is no flux. That is, $\langle\Delta t\rangle = 1/\Sigma_i \Gamma_i$ and

$$\sum_i \Gamma_i = 4\sum_{\ell=1}^{\ell_{\max}}\sum_{j=0}^{\ell-1}\binom{\ell}{j}\Gamma_\ell = \frac{4\Gamma_{00}e^{-\alpha}(1-\delta_{\ell\le\ell_{\max}})}{(1-2e^{-\alpha})(1-e^{-\alpha})}.$$

This gives

$$\langle\Delta t\rangle = \frac{(1-2e^{-\alpha})(1-e^{-\alpha})}{4\Gamma_{00}e^{-\alpha}(1-\delta_{\ell\le\ell_{\max}})}. \quad \text{(A9)}$$

If we focus on the number of neighbors considered by one diffusion event v, we note that while only four neighbors are accessible by a single hopping event on a cubic simple (100) surface, this number increases when long jumps are considered. Indeed, the nearest neighbor concept must be redefined since more than four sites are accessible. We must then consider all accessible neighbors, and weigh their contribution with respect to the standard four nearest neighbors. Thus, we can write

$$v_{\ell\le\ell_{\max}} = 4\sum_{\ell=1}^{\ell_{\max}}\frac{p_\ell}{p_1}\sum_{j=0}^{\ell-1}\binom{\ell}{j} = \frac{1}{\Gamma_{00}e^{-\alpha}\langle\Delta t\rangle}. \quad \text{(A10)}$$

Substituting the values of $\langle\Delta t\rangle$ and $v_{\ell\le\ell_{\max}}$ in Eq. (A8), the diffusion coefficient becomes

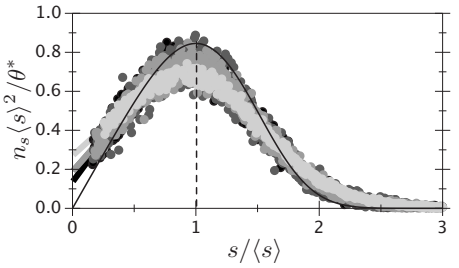

FIG. 17. Corrected island size distributions in the RA mode at $T=280$ K when the MNR applies. The correction was made by replacing the small island density by a linearly projected density from the left part of the distribution (thick lines in the figure). The theoretical curve of Amar and Family [36] for the IA mode is shown by a full light line. A broken vertical line indicates the average value of the distribution $(s/\langle s\rangle=1)$.

$$D_{\ell\leq\ell_{\max}}=\Gamma_{00}e^{-\alpha}\nu_{\ell\leq\ell_{\max}}.$$

We can write the diffusion coefficient for a jump extent limit with respect to the diffusion coefficient for single hopping events

$$D_{\ell\leq\ell_{\max}}=D_{\ell=1}\nu_{\ell\leq\ell_{\max}},$$

where $\nu_{\ell\leq\ell_{\max}}$ can be found from Eq. (A1). When there is no limit to the extent of a jump, the diffusion coefficient writes [28]

$$D_{\ell<\infty}=D_{\ell=1}\left(\frac{1-e^{-\alpha}-6e^{-3\alpha}+8e^{-4\alpha}}{[1-e^{-\alpha}]^2[1-2e^{-\alpha}]^2}\right).$$

APPENDIX B: EQUIVALENCE BETWEEN SIMULATIONS WITH DIFFERENT INITIAL PARAMETERS

In order to compare different simulations with the ones we performed and because the parameters used in Eqs. (1) and (2) are not well documented, we establish in this section conditions to obtain equivalent simulations. We begin by writing the rates of processes in two ways.

$$\Gamma_i=\Gamma_{00}e^{E_i/k_BT_{\rm iso}}e^{-E_i/k_BT}$$

and

$$\Gamma_i'=\Gamma_{00}'e^{E_i'/k_BT_{\rm iso}'}e^{-E_i'/k_BT'},$$

where the prime symbol is used to distinguish the two different simulations and we fixed $\varepsilon=\varepsilon'=1$ for two main reasons. (i) The assumption $\varepsilon=1$ is the most frequent in the literature, and (ii) equivalence conditions between simulations are by far more restrictive when $\varepsilon\neq 1$.

We demonstrate below that there exist conditions of temperatures and fluxes such that the nature and the order of the performed events would be exactly the same in both simulations if the same set of random numbers were used. If this is the case, the surface evolves identically in both cases even though the simulation time might be different, and we classify the simulations as "equivalent."

For simulations to be equivalent, the relative rates must be the same in both cases. Thus, $\Gamma_i/\Gamma_j=\Gamma_i'/\Gamma_j'$ for any i and j.

TABLE II. Equivalent temperatures for simulations with $T_{\rm iso}'=10T_{\rm iso}$.

T (K)	T' (K)
250	707
265	841
274	939
280	1014

This can only be achieved if $E_i'-E_j'=\omega(E_i-E_j)$ and yields a relation between T and T' as follows:

$$1/T-1/T_{\rm iso}=\omega(1/T'-1/T_{\rm iso}') \quad \text{(B1)}$$

where ω is a constant.

We then adjust the simulation time to allow the same number of events during the whole simulation in both cases. This number of events is the total simulation time divided by the average time between events. According to Eq. (11), we can write

$$t_{\rm tot}/\langle\Delta t\rangle=t_{\rm tot}'/\langle\Delta t'\rangle,$$

$$\frac{\theta(FabL_xL_y+\sum_i\Gamma_i)}{F}=\frac{\theta(F'abL_xL_y+\sum_i\Gamma_i')}{F'}. \quad \text{(B2)}$$

When we use temperatures according to Eq. (B1), we can derive the relationship between F and F' from Eq. (B2) as follows:

$$F/\Gamma_{00}=F'/\Gamma_{00}'e^{(\omega E_i-E_i')/k_B(1/T_{\rm iso}'-1/T')}, \quad \text{for any } i. \quad \text{(B3)}$$

We then analyze three precise cases: equivalence (i) between simulations with and without consideration of the MNR, (ii) between simulations with different isokinetic temperatures, and (iii) between simulations with proportional activation energies. We emphasize the fact that our definition of equivalence generally does not allow one to directly compare the results which depend on the time of simulation because this parameter is not the same from one simulation to the other.

1. Equivalence between simulations with and without consideration of the MNR

When the MNR is not considered, the isokinetic temperature is infinitely high, that is, $T_{\rm iso}'\to\infty$. If the activation en-

TABLE III. Equivalent temperatures for simulations with $E_i'=1.5E_i$ for any i of the bond counting model given by Eq. (3) and parameters of Sec. III.

T (K)	T' (K)
250	276
265	288
274	295
280	300

ergies are the same for both simulations, we obtain the two equivalence relations from Eqs. (B1) and (B3).

$$1/T = 1/T' + 1/T_{\mathrm{iso}} \tag{B4}$$

and

$$F/\Gamma_{00} = F'/\Gamma'_{00}. \tag{B5}$$

Thus, simulations for which the MNR applies or not, are equivalent when Eqs. (B4) and (B5) are verified. Equation (B4) indicates that in order to achieve equivalence, T' must rise much more rapidly than T. Therefore, many simulations which are not performed because the temperature is thought to be near some phase transition could become accessible when the MNR applies. In the rare case when the MNR is still valid above T_{iso}, the equivalence fails because T' must be negative.

With simulations that do not consider the MNR and use a prefactor $\Gamma'_{00}=2.203\times10^{9}$ s^{-1} as in Sec. IV A, we can obtain equivalent surfaces to those shown in Sec. IV B using the following parameters: $F'a^2=2203$ ML/s, $T'=887$, 1110, 1287, and 1431 K (instead of $Fa^2=0.1$ ML/s, $T=250$, 265, 274, and 280 K).

2. Equivalence between simulations with different isokinetic temperatures

When the MNR applies in both simulations with the same Γ_{00} value and identical activation energies, Eqs. (B1) and (B3) become

$$1/T = 1/T' + 1/T_{\mathrm{iso}} - 1/T'_{\mathrm{iso}} \tag{B6}$$

and

$$F = F'.$$

In this particular case, equivalent simulations also share an equivalent simulation time because $\Gamma_i=\Gamma'_i$ for any i. Moreover, for expressions of the form $e^{\sigma/T}$ such as the ones found in the diffusion coefficient equation, the global impact of Eq. (B6) is only a shift by the constant value $e^{\sigma(1/T_{\mathrm{iso}}-1/T'_{\mathrm{iso}})}$. For instance, if we had used an isokinetic temperature of $T'_{\mathrm{iso}}=10T_{\mathrm{iso}}$ (with $T_{\mathrm{iso}}=348.13$ K as given in Sec. III), we would have obtained the same values of α and $\nu_{\ell\leq\ell_{\max}}$ for the temperatures listed in Table II.

3. Equivalence between simulations with proportional activation energies

When the MNR applies in both simulations with the same Γ_{00} value, the same isokinetic temperature and activation energies that respect a direct proportional relation ($E'_i=\omega E_i$ for all i), Eqs. (B1) and (B3) become

$$1/T = \omega/T' + (1-\omega)1/T_{\mathrm{iso}}$$

and

$$F = F'.$$

Again, in this case, equivalent simulations also share an equivalent simulation time because $\Gamma_i=\Gamma'_i$ for any i. As an example, for activation energies 1.5 times those used in this study [Sec. III and Eq. (3)], equivalent temperatures that give the same α and $\nu_{\ell\leq\ell_{\max}}$ values are listed in Table III.

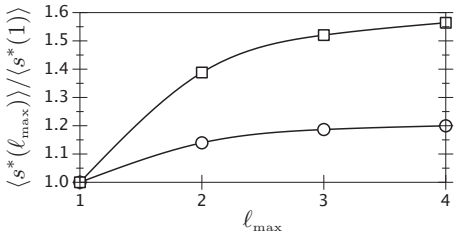

FIG. 18. Evolution of the average size of large islands normalized with respect to the value obtained for $\ell_{\max}=1$. The circles are associated to the IA mode (in which case $\langle s\rangle=\langle s^*\rangle$ since there is only one mode in the island size distribution) while the squares are related to the RA mode results where we corrected the density of small islands to discard an important effect due mostly to reversible aggregation. The solid lines are guidelines to the eye. The MNR is considered.

APPENDIX C: SYNERGISTIC EFFECTS BETWEEN REVERSIBLE AGGREGATION AND LONG JUMPS

Let us study a particular case to show that synergistic effects are found between reversible aggregation and long jumps. At $T=280$ K in the RA mode when the MNR applies, we have shown that we obtain a bimodal island size distribution (see Fig. 11). The small island mode is mainly affected by the RA mode since little variation is found when the jump extent limit varies. Thus, we can eliminate an important part of the effect of the RA mode by making a linear regression on the large island mode. We can perform this task by retracting the small island mode and replacing it by a linear projection of island density towards small densities as shown in Fig. 17.

This procedure, while approximative, can give some insight on the large island size distribution. In Fig. 17, $\langle s\rangle$ is the average size of large islands found with the corrected distribution. Since some atoms were eliminated through this correction, the coverage θ has been modified accordingly (we note θ^* this effective coverage). When $\ell_{\max}$ passes from 1 to 4, θ^* takes the following values (in ML): 0.187, 0.188, 0.188, and 0.188. We readily see that most of the adatoms are found in the large island mode since $\theta=0.2$ ML.

We see, in Fig. 17, that the island size distributions for $\ell_{\max}$ ranging from 1 to 4 are mostly superimposed and are coherent with the model of Amar and Family [36]. If linearly additive effects between the reversible aggregation and long jumps are to be observed, we expect the corrected average size of those new distributions ($\langle s^*\rangle=\langle s\rangle\theta/\theta^*$) to be mainly affected by the jump extent limit. That is, we expect $\langle s^*\rangle$ to evolve as $\langle s\rangle$ evolves in the IA mode (see Fig. 8). Figure 18 compares those two evolutions (a normalization is made with respect to the corrected average island size for $\ell_{\max}=1$).

We clearly see that increasing the jump extent limit from 1 to 4 implies an increase of 20% of the average island size in the IA mode, while this increase is more than 56% in the RA mode. Therefore, some synergistic effects happen be-

tween the reversible aggregation and long jumps. We can explain this by the fact that the larger diffusion coefficient due to long jumps allows detached atoms to reach large islands and increase their size. Because of the strong RA mode, other adatoms detach frequently enough from island edge to compensate this attachment. Note that we observe the same trend if we compare the evolution of the large island modes instead of the large island correct average sizes.

[1] P. Hanggi, P. Talkner, and M. Borkovec, Rev. Mod. Phys. **62**, 251 (1990).

[2] G. Boisvert, L. J. Lewis, and A. Yelon, Phys. Rev. Lett. **75**, 469 (1995).

[3] (a) A. Yelon and B. Movaghar, Phys. Rev. Lett. **65**, 618 (1990); (b) A. Yelon, B. Movaghar, and H. M. Branz, Phys. Rev. B **46**, 12244 (1992).

[4] A. Yelon, B. Movaghar, and R. S. Crandall, Rep. Prog. Phys. **69**, 1145 (2006).

[5] J. Jacobsen, K. W. Jacobsen, and J. P. Sethna, Phys. Rev. Lett. **79**, 2843 (1997).

[6] F. Montalenti and R. Ferrando, Phys. Rev. B **59**, 5881 (1999).

[7] R. Ferrando, R. Spadacini, G. E. Tommei, and G. Caratti, Surf. Sci. **311**, 411 (1994).

[8] L. Y. Chen and S. C. Ying, Phys. Rev. B **60**, 16965 (1999).

[9] (a) B. Borovsky, M. Krueger, and E. Ganz, Phys. Rev. B **59**, 1598 (1999); (b) J. C. Hamilton, M. R. Sørensen, and A. F. Voter, *ibid.* **61**, R5125 (2000); (c) D. C. Senft, Appl. Surf. Sci. **94/95**, 231 (1996); (d) D. C. Senft and G. Ehrlich, Phys. Rev. Lett. **74**, 294 (1995).

[10] (a) G. Antczak and G. Ehrlich, Phys. Rev. Lett. **92**, 166105 (2004); (b) G. Antczak and G. Ehrlich, Phys. Rev. B **71**, 115422 (2005).

[11] G. Antczak and G. Ehrlich, Surf. Sci. Rep. **62**, 39 (2007).

[12] G. Boisvert and L. J. Lewis, Phys. Rev. B **54**, 2880 (1996).

[13] C. Ratsch, A. Zangwill, P. Šmilauer, and D. D. Vvedensky, Phys. Rev. Lett. **72**, 3194 (1994).

[14] G. S. Bales and A. Zangwill, Phys. Rev. B **55**, R1973 (1997).

[15] E. G. Seebauer and C. E. Allen, Prog. Surf. Sci. **49**, 265 (1995).

[16] S. H. Payne, J.-S. McEwen, H. J. Kreuzer, and D. Menzel, Surf. Sci. **594**, 240 (2005).

[17] H. Pfnür, P. Feulner, and D. Menzel, J. Chem. Phys. **79**, 4613 (1983).

[18] E. D. Westre, D. E. Brown, J. Kutzner, and S. M. George, Surf. Sci. **302**, 280 (1994).

[19] (a) K. Sinniah, M. G. Sherman, L. B. Lewis, W. H. Weinberg, J. T. Yates, Jr., and K. C. Janda, Phys. Rev. Lett. **62**, 567 (1989); (b) G. A. Reider, U. Höfer, and T. F. Heinz, *ibid.* **66**, 1994 (1991); (c) D. A. Hansen, M. R. Halbach, and E. G. Seebauer, J. Chem. Phys. **104**, 7338 (1996).

[20] (a) P. W. Tamm and L. D. Schmidt, J. Chem. Phys. **54**, 4775 (1971); (b) S. C. Wang and R. Gomer, *ibid.* **83**, 4193 (1985); (c) M. Tringides and R. Gomer, Surf. Sci. **155**, 254 (1985).

[21] (a) G. Henkelman and H. Jónsson, Phys. Rev. Lett. **90**, 116101 (2003); (b) F. Montalenti, Surf. Sci. **543**, 141 (2003).

[22] T. R. Linderoth, S. Horch, E. Lægsgaard, I. Stensgaard, and F. Besenbacher, Phys. Rev. Lett. **78**, 4978 (1997).

[23] The concept of long jump extent limit $\ell_{\max}$ signifies that all jumps with an extent up to $\ell_{\max}$ are considered.

[24] L. Y. Chen, M. R. Baldan, and S. C. Ying, Phys. Rev. B **54**, 8856 (1996).

[25] (a) P. Šmilauer, M. R. Wilby, and D. D. Vvedensky, Phys. Rev. B **47**, 4119 (1993); (b) T. Kaneko, P. Šmilauer, B. A. Joyce, T. Kawamura, and D. D. Vvedensky, Phys. Rev. Lett. **74**, 3289 (1995).

[26] R. L. Schwoebel and E. J. Shipsey, J. Appl. Phys. **37**, 3682 (1966).

[27] G. Ehrlich and F. G. Huda, J. Chem. Phys. **44**, 1039 (1966).

[28] If the path multiplicity is not considered, the diffusion coefficient is $D_{\ell<\infty}=D_{\ell=1}((1+e^{-\alpha})/(1-e^{-\alpha}))^2$, which should be compared to the theoretical result of Boisvert and Lewis [12] in one dimension in which we apply explicitly the MNR, that is $D_{\ell<\infty}=D_{\ell=1}(1+e^{-\alpha})/(1-e^{-\alpha})$.

[29] T. Ala-Nissila, R. Ferrando, and S. C. Ying, Adv. Phys. **51**, 949 (2002).

[30] A. B. Bortz, M. H. Kalos, and J. L. Lebowitz, J. Comput. Phys. **17**, 10 (1975).

[31] S. E. Koonin and D. C. Meredith, *Computational Physics* (Addison-Wesley, Reading, MA, 1990).

[32] M. Matsumoto and T. Nishimura, ACM Trans. Model. Comput. Simul. **8**, 3 (1998).

[33] W. Zhu, F. B. de Mongeot, U. Valbusa, E. G. Wang, and Z. Zhang, Phys. Rev. Lett. **92**, 106102 (2004).

[34] U. Kürpick and T. S. Rahman, Phys. Rev. B **57**, 2482 (1998).

[35] (a) G. Schulze Icking-Konert, M. Giesen, and H. Ibach, Surf. Sci. **398**, 37 (1998); (b) P. J. Feibelman, Phys. Rev. Lett. **81**, 168 (1998); (c) Y. Li and A. E. DePristo, Surf. Sci. **319**, 141 (1994); (d) M. Giesen and H. Ibach, Surf. Sci. **431**, 109 (1999).

[36] J. G. Amar and F. Family, Phys. Rev. Lett. **74**, 2066 (1995).

[37] The most frequent size of large islands (s_{mod}) is found by fitting a second order curve on the mode of largest islands in the island size distribution. It gives an insight of the value of the mode, but is quite approximative since some island size distributions are sparse. This does not mean that the large island mode does not exist. In fact, this mode is large, but still well defined, provided many simulation results are averaged.

[38] $\langle s_c \rangle$ is used instead of $\langle s \rangle$ to illustrate the average size of stable islands. The relationship between the two parameters is $\langle s_c \rangle n_{\mathrm{isl}}+n_{\mathrm{ad}}=\langle s \rangle (n_{\mathrm{ad}}+n_{\mathrm{isl}})$, with n_{ad} and n_{isl} the adatom and stable island densities.

[39] M. R. Sørensen and A. F. Voter, J. Chem. Phys. **112**, 9599 (2000).

[40] V. I. Melnikov, Phys. Rev. E **48**, 3271 (1993).

[41] L. Kuipers and R. E. Palmer, Phys. Rev. B **53**, R7646 (1996).

[42] A. Zangwill and E. Kaxiras, Surf. Sci. **326**, L483 (1995).

[43] M. Meixner, E. Schöll, V. A. Shchukin, and D. Bimberg, Phys. Rev. Lett. **87**, 236101 (2001).

[44] G. Boisvert and L. J. Lewis, Phys. Rev. B **56**, 7643 (1997).

[45] M. Marinica, C. Barreteau, M.-C. Desjonquères, and D. Spanjaard, Phys. Rev. B **70**, 075415 (2004).

[46] K. Kyuno and G. Ehrlich, Surf. Sci. **437**, 29 (1999).

[47] C. M. Chang, C. M. Wei, and S. P. Chen, Phys. Rev. Lett. **85**, 1044 (2000).